International Journal of Numerical Methods for Heat & Fluid Flow

2325

Received 31 March 2025
Revised 22 August 2025
Accepted 16 October 2025

Thermal management of cylindrical lithium-ion batteries using internal and external phase change material placement

Francesco Piccirillo, Marcello Iasiello and Nicola Bianco
Department of Industrial Engineering, Università Degli Studi di Napoli Federico II, Napoli, Italy, and

Wilson K.S. Chiu
School of Mechanical, Aerospace and Manufacturing Engineering, University of Connecticut, Storrs, Connecticut, USA

Abstract

Purpose – Thermal management is essential to ensure the performance and safety of lithium-ion batteries, and effective heat dissipation helps prevent excessive temperature rise. This study aims to explore advanced passive thermal management strategies by developing a coupled electrochemical–thermal model to investigate the effectiveness of different phase change material (PCM) configurations: internal (within a hollow mandrel), external (surrounding the cell) and combined internal/external placement. The objective is to contain temperature rise while optimizing battery pack dimensions. In addition, a parametric analysis on the external PCM thickness is carried out to identify optimal design solutions for space-constrained applications.

Design/methodology/approach – An 18650 lithium cobalt oxide (LCO) battery (3.7 V, 2.6 Ah) is studied, combining a multiscale pseudo-two-dimensional electrochemical model with a two-dimensional axis-symmetric thermal domain. Sodium thiosulfate pentahydrate is selected as PCM and modeled with an enthalpy-based method to account for latent heat effects. Equal PCM volume is used to compare internal and external configurations.

Findings – The internal/external PCM configuration delays the battery critical temperature of 50 °C by up to 120.5%, compared to the case without PCM. External- and internal-only PCM provide delays of 58.6% and 40.5%, respectively. The parametric study shows that, to maintain a safe operating temperature of 45°C, an optimal PCM thickness of 1.66 mm is required for the internal/external layout versus 1.96 mm for the external-only case, corresponding up to a 5.4% battery pack volume saving.

Originality/value – This work highlights the benefit of internal PCM integration in lithium-ion batteries, improving both thermal buffering and spatial efficiency. The findings offer guidance for designing compact, passively cooled battery systems.

Keywords Lithium-ion battery, Thermal model, Phase change material, Battery thermal management

Paper type Research paper

International Journal of Numerical Methods for Heat & Fluid Flow
Vol. 36 No. 6, 2026
pp. 2325-2357
Emerald Publishing Limited
0961-5539
DOI 10.1108/HFF-03-2025-0212

Nomenclature

Symbols

Latin

A = area [m^2];
Bi = Biot number [/];
C = capacity [Ah];
c = specific heat [$J/(kg \cdot K)$];
c_e = concentration in the electrolyte phase [mol/m^3];
c_s = concentration in the solid phase [mol/m^3];
D = diffusion coefficient [m^2/s];
d = thickness [m];
E = energy [J/mol];
F = Faraday's constant [C/mol];
$f_{\pm}$ = mean molar activity coefficient [/];
g = gravity acceleration [m/s^2];
H_l = latent heat of fusion [J/kg];
h = convective heat transfer coefficient [$J/(m^2 \cdot K)$];
I = improvement [%];
i = Interfacial current density [A/m^2];
i_0 = Exchange current density [A/m^2];
k = thermal conductivity [$W/(m \cdot K)$];
k_0 = kinetic rate constant [m/s];
L = characteristic length [m];
l = height [m];
Nu = Nusselt number [/];
Pr = Prandtl number [/];
$\dot{Q}$ = heat generation [W/m^3];
R = universal gas constant [$J/(mol \cdot K)$];
R_s = solid phase particle radius [m];
r = radial coordinate [m];
Ra = Raileigh number [/];
S_h = latent heat term [W/m^3];
T = temperature [K];
t = time [s];
t_{Li^+} = electrolyte ionic current fraction by lithium ions [/];
U = voltage [V];
V = volume [m^3];
x = axial coordinate [m]; and
z = axial coordinate [m].

Greek

α = thermal diffusivity [m^2/s];
α_a = transfer coefficient [/];
β = thermal expansion coefficient [1/K];
ε = volume fraction [/];
η = overpotential [V];
θ = angular coordinate [rad];
ν = kinematic viscosity [m^2/s];
ρ = density [kg/m^3];

σ = electrical conductivity [S/m];
φ = electric potential [V];
χ = correction factor [/]; and
ψ = liquid phase fraction [/].

Subscripts

a = anodic
act = activation;
amb = ambient;
ap = applied;
av = average;
c = cathodic
cc = current collector;
co = core;
n = negative;
e = electrolyte;
ele = electrode;
eq = equilibrium;
f = film;
gen = generation;
jou = Joule;
l = liquid;
lim = limit;
man = mandrel;
max = maximum;
n = negative;
nom = nominal;
op = operational;
opt = optimal;
p = positive;
ref = reference;
RL = representative layer;
s = solid phase;
sav = saving;
sep = separator;
sol = solidification; and
sur = surface.

Superscripts

eff = effective.

Acronyms

BMS = battery management system;
LCO = lithium cobalt oxide;
LIB = lithium ion battery;
P2D = pseudo-two-dimensional;
PCM = phase change material;
RMS = root mean square;
SoC = state of charge;

SPM = single particle model; and
TR = thermal runaway.

1. Introduction

The rapid advancement of electrification technologies has placed lithium-ion batteries (LIBs) at the center of modern energy solutions, particularly in the fields of electric mobility (Veza *et al.*, 2024) and renewable energy storage (Yang *et al.*, 2018). Despite their high energy density, efficiency and cycle life, LIBs face critical challenges related to thermal management. Excessive heat generation during high charge/discharge cycles can lead to capacity fade (Atalay *et al.*, 2020), performance loss and, in extreme cases, thermal runaway (TR) (Feng *et al.*, 2019; Mallick and Gayen, 2023), posing significant safety risks.

1.1 State of the art and motivation

To prevent thermal problems due to battery overheating, different multi-physical models are proposed to predict heat generation within the battery, so that the appropriate thermal management system for the battery pack can be designed. Models must be multi-physical, as their thermal generation depends on electrical or chemical parameters (Jordan *et al.*, 2024). The models can be multi-dimensional, to correctly describe the behavior of the cell, or compact and fast, that can be integrated into battery management systems (BMSs) (Li *et al.*, 2020). Multi-dimensional battery models are primarily classified as electro-thermal or electrochemical–thermal. Electro-thermal models estimate heat generation using equivalent electrical circuit parameters, such as Thevenin-based models, which represent battery behavior through an equivalent electrical circuit (Nikolian *et al.*, 2016). In contrast, electrochemical–thermal models use governing equations to analyze the lithium-ion concentration within the battery, enabling a multi-scale analysis: from the microscale of electrode solid particles to the macroscale of the entire cell. Both types of models share a common approach to heat generation calculation, which is based on the formulation proposed by (Bernardi *et al.*, 1985). This method accounts for a reversible heat component, which arises due to entropy variations within the system. This entropy-related heat contribution depends on the state of charge (SoC) and the entropy coefficient, and it influences the overall thermal behavior of the battery during charge and discharge cycles. Notably, the entropy coefficient can assume positive or negative values depending on the SoC and whether the battery is charging or discharging. Consequently, the sign of the reversible heat term also changes, leading to either a reduction or an increase in the total heat generation. One of the most widely adopted electrochemical–thermal models is the pseudo-two-dimensional (P2D) model (Doyle *et al.*, 1993; Fuller *et al.*, 1994), which provides a detailed representation of electrode kinetics and transport phenomena, or the single particle model (SPM) (Zhang *et al.*, 2000) which is a model simplification, assuming that the concentration of lithium ions in the liquid phase is uniform throughout the battery, and the electric potential of the solid phase is uniform across the electrode. Different P2D model simplifications are proposed to improve simulation time (Jokar *et al.*, 2016). For compact and fast models, the approach is primarily based on electrical parameters and are an optimal solution for temperature prediction in a real-time analysis. In this case, the lumped model (Catalano *et al.*, 2023) can be used to reduce computational time. Also, innovative batteries such as sodium-sulfur batteries are studied through a lumped thermal model (Csemány, 2025).

To mitigate temperature issues, effective thermal management strategies are essential to maintain optimal operating temperatures, avoid the hotspot that can lead to thermal runaway (Afzal *et al.*, 2022) and enhance both battery lifespan and efficiency (Lin *et al.*, 2021). Various approaches have been proposed, including air (Chen *et al.*, 2024a), and liquid cooling systems (Wu *et al.*, 2024), heat pipes (Su *et al.*, 2025) and advanced thermal interface materials (Lee *et al.*, 2023). An emerging approach are dielectric fluids thermal management, Menale *et al.* (2019)

analyzed two different dielectric liquids, Clearco-50cSt and Galden HT135 and compared them to air, proving that Galden HT135 is an efficient liquid for thermal management, while Williams *et al.* (2024) studied the phase change process under pool boiling conditions for a dielectric immersion cooling with Novec 7000. Also, passive and hybrid thermal management solutions (Zhao *et al.*, 2020) are gaining increasing attention for their ability to balance thermal performance with space and energy efficiency, making them particularly attractive for electric vehicle and stationary storage applications. Finally, one of the most studied passive solutions is with phase change materials (PCM) (Pilali *et al.*, 2025), leveraging their ability to absorb and store heat through latent heat during phase transition. Unlike conventional cooling methods, phase change materials offer intrinsic temperature stabilization during their solid-to-liquid transition. As the battery generates heat during operation, this thermal energy is absorbed by the PCM in the form of latent heat. While absorbing heat, the PCM remains at its nearly-constant phase change temperature, which limits the heat accumulation in the battery itself and reduces its temperature rise. Recent studies have investigated the enhancement of PCM thermal conductivity via the addition of nanoparticles, giving rise to nano-enhanced PCM. For instance, a numerical–experimental study on 18,650 Li-ion cells was conducted using paraffin wax combined with different nanoparticles such as CuO, Al_2O_3 and TiO_2 at varying concentrations to improve heat dissipation (Vyas *et al.*, 2024). Also with this application, different hybrid solutions are proposed (Khan *et al.*, 2023), for example with fins (Zhang *et al.*, 2023), metal foam integration (Buonomo *et al.*, 2018) or honeycomb structures (Sutheesh *et al.*, 2024; Chen *et al.*, 2024b). For instance, a hybrid BTMS combining PCM with a liquid-cooled plate arranged in a honeycomb configuration has been proposed for cylindrical cells, showing improved temperature uniformity and dissipation effectiveness through 3D simulations (Zhuang *et al.*, 2021). However, these approaches typically require external structural elements, increasing the system's size and complexity. In contrast, this study introduces a novel passive cooling configuration by integrating PCM internally inside the battery's hollow mandrel, without increasing the external footprint. This internal PCM can be combined with a standard external PCM layer to create a hybrid layout that maximizes battery thermal dissipation. This is an opportunity to investigate such configurations using a coupled electrochemical–thermal model. This approach is of particular interest for compact systems, such as portable electronics and electric vehicles, where space is a critical constraint.

1.2 Aim of this study

To address the associated challenges, a multiscale coupled electrochemical–thermal model of a lithium cobalt oxide (LCO) 18650 cylindrical battery is developed to investigate the thermal behavior under different passive thermal management configurations. The analysis focuses on three PCM arrangements: internal (within the mandrel), external (surrounding the cell) and a combined internal/external layout, assessing their effectiveness in containing temperature rise while minimizing the impact on the battery pack volume. The PCM analyzed is an inorganic compound, the sodium thiosulphate pentahydrate, the electrochemical model is based on the pseudo-two-dimensional approach, while the thermal model is treated as two-dimensional, leveraging symmetry along the angular direction. These strategies offer significant advantages in heat dissipation compared to a battery without PCM, with the internal PCM approach also providing space optimization benefits, allowing for the development of more compact battery packs. In addition, a parametric study on PCM external thickness is conducted to determine the optimal PCM layer required to maintain the battery's operating temperature below two critical thresholds: a battery temperature limit of 50°C (Rodrigues *et al.*, 2017; Jiang *et al.*, 2020), as recommended by manufacturers to prevent accelerated

aging and thermal runaway, and an operational temperature limit of 45°C, set to provide a safety margin and avoid approaching the maximum threshold too closely. This conservative limit also accounts for the progressive aging of the cell, which may lead to reduced thermal performance over time and an increased electrical resistance – an aspect not foreseen by the thermal management system – thus justifying the degree of thermal oversizing to ensure long-term reliability. This analysis is performed for both the external-only and internal/external PCM configurations, highlighting the potential space-saving benefits of a combined PCM approach.

The main research gaps and objectives of this study are summarized as follows:

- *Gap 1:* Most existing works on PCM-enhanced thermal management focus on external-only or hybrid solutions (e.g. fins, metal foams), which increase the overall battery footprint.
- *Gap 2:* The spatial efficiency of internal PCM configurations in cylindrical cells remains underexplored in comparison to more conventional external PCM approaches.
- *Objective 1:* To develop a fully coupled electrochemical–thermal model that captures both cell dynamics and PCM phase change effects with internal/external placement.
- *Objective 2:* To compare the thermal performance of internal, external and combined PCM configurations under identical volume and thermal boundary conditions.
- *Objective 3:* To assess the potential space savings in percentage terms and thermal benefits of internal PCM via a parametric analysis on PCM thickness.

This approach aims to support the design of compact and thermally stable battery systems, particularly for high energy density applications such as electric mobility and portable electronics.

2. Electrochemical–thermal model

In this section, the coupled electrochemical–thermal model of the battery and the thermal model for the phase change material are presented. The electrochemical–thermal model integrates a pseudo-two-dimensional electrochemical framework to simulate the internal electrochemical reactions, with a two-dimensional axisymmetric thermal model to predict heat generation Q and evaluate temperature distribution T within the battery. The interaction between these models enables a comprehensive analysis of the battery's thermal response under various operating conditions. The coupling method between the models is also analyzed, showing how certain electrochemical parameters, such as the electrolyte diffusion coefficient D_e, the electrolyte conductivity σ_e, the mean molar activity coefficient $f_\pm$ and the potential equilibrium U_{eq}, are temperature-dependent and affect the calculation of heat generation Q within the battery core, leading to a non-linearity of the problem. Meanwhile, the thermal behavior of the phase change material is described by an enthalpy-based model that accounts for latent heat absorption and release during phase transitions. A commercial finite element analysis solver, COMSOL Multiphysics, was used for this analysis.

2.1 Electrochemical model

A lithium-ion battery is composed of multiple repeating layers of current collectors, electrodes and separators, which are tightly wound into a cylindrical structure known as a "jelly roll". The layers are typically wrapped around a support structure called mandrel, to provide mechanical stability. In this design, both the positive and negative current collectors

are coated of their respective electrode, forming a compact, multi-layered configuration that enhances energy density. During charge and discharge, lithium ions migrate between the two electrodes. The model uses a pseudo-two-dimensional (P2D) approach (Doyle *et al.*, 1993; Fuller *et al.*, 1994), incorporating two interconnected spatial dimensions, as illustrated in Figure 1 during a discharge. The first dimension, x, represents the cell thickness and captures charge and mass transport in the electrodes and electrolyte, along with the electrochemical reactions at the electrode-electrolyte interface. The second dimension corresponds to the particle radius r and is used to solve the lithium diffusion equations within the electrode's active material in spherical coordinates. This coupled approach enables a detailed representation of both macroscopic and microscopic transport phenomena within the battery. To enhance computational efficiency, the following assumptions are introduced:

- Current distribution is considered one-dimensional along the x-direction.

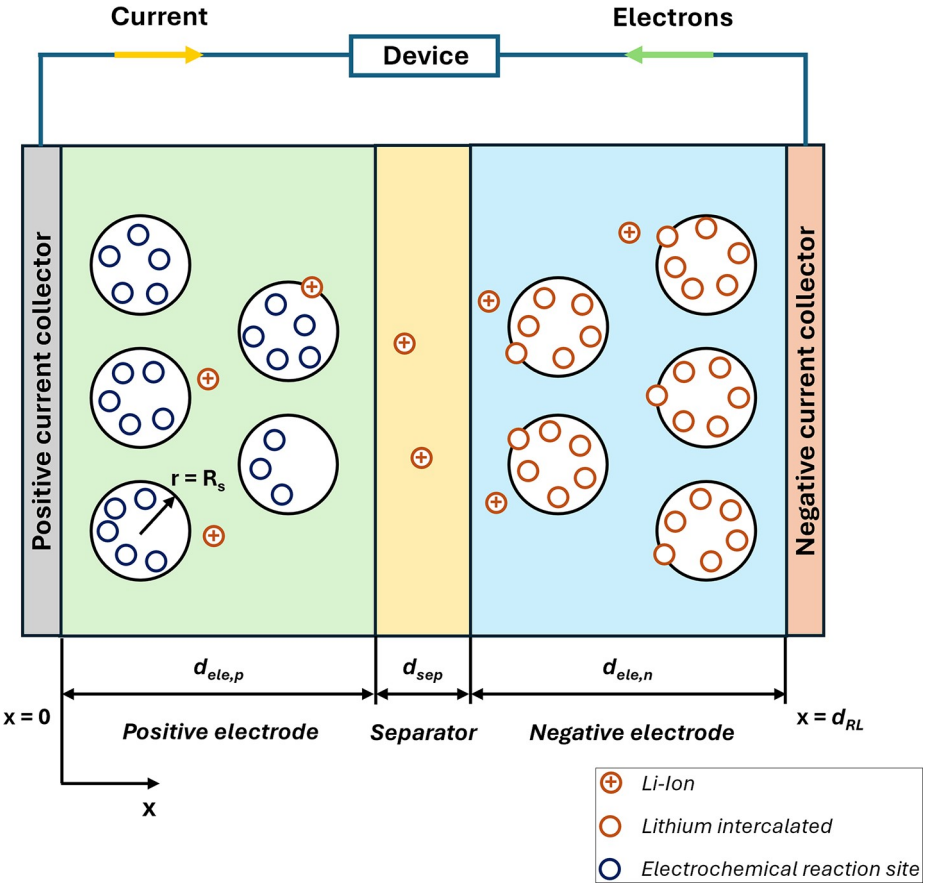

Figure 1. Representation of the interconnected dimensions for the pseudo-two-dimensional model during a discharge: x, for the cell thickness and r, for the particle radius

- The current collectors are assumed to have sufficiently high electrical conductivity σ, ensuring a homogeneous potential distribution along the x-direction.
- The active material particles in the electrodes are considered to have a uniform size distribution with the same particle radius R_s.
- Side reactions and gas generation during electrochemical processes are neglected.

Due to the second assumption, the electrochemical model does not include the current collectors, and no electrochemical reactions are present within them. As a result, the model does not account for the ohmic drop along with the current collectors. However, these components will be incorporated into the thermal model. The electrochemical computational domain includes only a representative layer, consisting of a single layer of each component. This simplification is justified by the assumption that all layers exhibit identical behavior. In the figure below, $d_{ele,p}$, d_{sep} and $d_{ele,n}$ represent the positive electrode, separator and negative electrode thickness, while $d_{RL} = d_{ele,p} + d_{sep} + d_{ele,n}$ is the total thickness of the representative layer.

2.1.1 Mass conservation equations. During the discharging process, lithium ions migrate from the negative electrode to the positive electrode, passing through the electrolyte. This process reversed during charge. The concentration of lithium ions in the solid phase c_s, within both electrodes is governed by the mass conservation equation. It is expressed as a function of the radial coordinate r within a spherical particle and time t:

$$\frac{\partial c_s}{\partial t} = \frac{D_s}{r^2}\frac{\partial}{\partial r}\left(r^2\frac{\partial c_s}{\partial r}\right) \quad r \in [0, \quad R] \tag{1}$$

where D_s is the diffusion coefficient within the solid phase. As a boundary condition for the spherical particle, two Neumann conditions are used at the particle center [equation (2)] and at the particle surface [equation (3)]. In the first one, a symmetry condition is imposed at the particle center, ensuring that there is no net lithium flux at $r = 0$. Since the diffusion process is radially symmetric, there is no preferential direction for lithium movement at the core, leading to a zero-concentration gradient. The second boundary condition links the lithium flux at the particle surface to the electrochemical reaction occurring at the electrode–electrolyte interface, ensuring that lithium flux at the surface matches the rate at which lithium is inserted into or extracted from the particle due to the applied current:

$$\left(\frac{\partial c_s}{\partial r}\right)_{r=0} = 0 \tag{2}$$

$$\left(-D_s\frac{\partial c_s}{\partial r}\right)_{r=R_s} = \frac{i}{F} \tag{3}$$

where i represents the interfacial current density and F is the Faraday's constant.

As initial condition, a homogeneous concentration in the solid particle $c_{s,0}$ is imposed. In Figure 2, a schematic representation of the boundary conditions for the lithium-ion concentration within the solid phase is shown.

The concentration of lithium ions in the electrolyte c_e, varies as a function of both cell thickness x and time t. It is described through equation (4) that represents the conservation of lithium ions in the electrolyte phase:

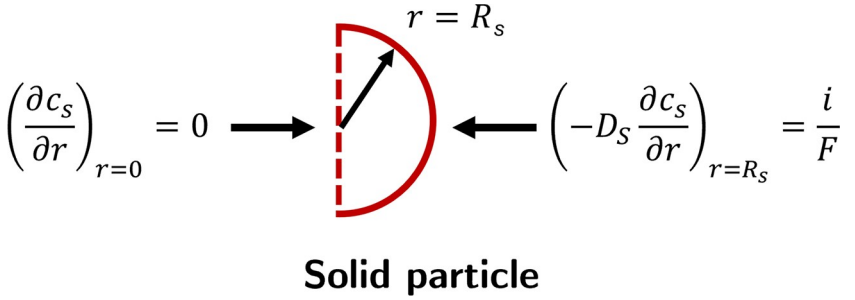

Figure 2. Schematic representation of the boundary conditions for the lithium-ion concentration within the solid phase

$$\varepsilon_e \frac{\partial c_e}{\partial t} = \frac{\partial}{\partial x}\left(D_e^{eff} \frac{\partial c_e}{\partial x}\right) + (1 - t_{Li^+}) \frac{A_s i}{F} \qquad x \in [0, \ d_{RL}] \tag{4}$$

It consists of the following key terms:

- *Time-dependent term* $\varepsilon_e \frac{\partial c_e}{\partial t}$: representing the accumulation or depletion of lithium ions in the electrolyte over time, where ε_e is the electrolyte volume fraction, which varies across the battery components, accounting that only a portion of the battery's volume is occupied by the electrolyte.
- *Diffusive term* $\frac{\partial}{\partial x}\left(D_e^{eff} \frac{\partial c_e}{\partial x}\right)$: describing how lithium ions diffuse through the electrolyte, driven by concentration gradients. where D_e^{eff} is the effective diffusion coefficient that accounts for the presence of a porous structure composed of the electrodes and the separator, which affects ion movement. For this reason, the effective diffusion coefficient D_e^{eff} is given by the following equation:

$$D_e^{eff} = D_e \varepsilon_e^p \tag{5}$$

where D_e is the intrinsic diffusion coefficient of lithium ions in the electrolyte and p is the Bruggeman porosity exponent, assumed to be 1.5 for both electrodes and the separator. This empirical factor accounts for the tortuous pathways that lithium ions follow in a porous medium, reducing the effective diffusivity compared to a bulk electrolyte. This formulation ensures that the transport properties of lithium ions are correctly adjusted based on the microstructure of the battery materials:

- *Source term* $(1 - t_{Li^+}) \frac{A_s i}{F}$: representing the effect of electrochemical reactions at the electrode-electrolyte interface, where t_{Li^+} is defined as the fraction of the total ionic current in the electrolyte that is carried by lithium ions, assuming a uniform electrolyte composition and A_s is the specific interfacial area, defined in equation (6), that scales the reaction rate by representing the available active surface for lithium-ion exchange at the electrode-electrolyte interface:

$$A_s = \frac{3\varepsilon_s}{R_s} \tag{6}$$

where ε_s represents the volume fraction occupied by the solid phase within the porous electrode.

At both ends of the electrolyte domain, $x = 0$ and $x = d_{RL}$, there is a Neumann's boundary condition assuming no flux of lithium ions:

$$\left(D_e^{eff}\frac{\partial c_e}{\partial x}\right)_{x=0} = \left(D_e^{eff}\frac{\partial c_e}{\partial x}\right)_{x=d_{RL}} = 0 \tag{7}$$

These boundary conditions indicate that lithium ions are not lost or gained at the boundaries, ensuring conservation of mass. Physically, this implies that the electrodes act as barriers, preventing lithium-ion diffusion beyond the defined electrolyte region. In the region between the electrodes and the separator, Li-ion concentration is assumed continuous across the surfaces. As an initial condition, a homogeneous concentration in the electrolyte $c_{e,0}$ is settled.

2.1.2 Charge conservation equations. The potential within the solid phase φ_s obeys the charge conservation equation through Ohm's law, which can be expressed as in equation (8):

$$\frac{\partial}{\partial x}\left(\sigma_s^{eff}\frac{\partial \varphi_s}{\partial x}\right) = A_s i \tag{8}$$

where σ_s^{eff} represents the effective electrical conductivity of the solid phase, as it depends on the porous structure and it is corrected through the Bruggeman coefficient p equal to 1.5 and $\sigma_s^{eff} = \sigma_s \varepsilon_s^p$, where σ_s is the intrinsic electrical conductivity of the active material. The boundary conditions governing this equation are:

- At the interface between the positive electrode and the positive current collector, $x = 0$, all the applied current is transported through the solid particles that coat the current collector:

$$\left(-\sigma_s^{eff}\frac{\partial \varphi_s}{\partial x}\right)_{x=0} = i_{ap} \tag{9}$$

where i_{ap} is the applied current density per unit area of the positive electrode plate:

- At the interface between the negative electrode and the negative current collector, $x = d_{RL}$, a Dirichlet boundary condition with a zero-potential for a grounded reference condition:

$$(\varphi_s)_{x=d_{RL}} = 0 \tag{10}$$

- At the interfaces between the electrodes and the separator (i.e. $x = d_{ele,p}$, $x = d_{RL} - d_{ele,n}$), charge transport occurs exclusively through the electrolyte, leading to a Neumann boundary condition, with a zero-flux condition at the electrode–separator interfaces. This occurs because, at these locations, the charge is no longer transported through the solid phase but rather through the electrolyte:

$$\left(-\sigma_s^{eff}\frac{\partial\varphi_s}{\partial x}\right)_{x=d_{ele,p}} = \left(-\sigma_s^{eff}\frac{\partial\varphi_s}{\partial x}\right)_{x=d_{RL}-d_{ele,n}} = 0 \tag{11}$$

As initial conditions, the solid-phase potential φ_s is set equal to the equilibrium potential U_{eq} throughout the positive electrode thickness $d_{ele,p}$, while a reference solid-phase zero-potential φ_s is imposed across the negative electrode thickness $d_{ele,n}$.

The potential in the electrolyte phase φ_e is governed by the following equation:

$$\frac{\partial}{\partial x}\left(\sigma_e^{eff}\frac{\partial\varphi_e}{\partial x}\right) - \frac{\partial}{\partial x}\left(\frac{2RT\sigma_e^{eff}}{F}(1-t_{Li^+})\left(1+\frac{d(\ln f_\pm)}{d(\ln c_e)}\right)\left(\frac{\partial \ln c_e}{\partial x}\right)\right) + A_s i = 0 \tag{12}$$

This equation consists of three main contributions:

(1) *The conductive term* $\frac{\partial}{\partial x}\left(\sigma_e^{eff}\frac{\partial\varphi_e}{\partial x}\right)$: Describing ionic charge transport by conduction within the electrolyte, driven by the electric potential gradient $\frac{\partial\varphi_e}{\partial x}$. The effective ionic conductivity of the electrolyte σ_e^{eff} is affected from porosity and tortuosity effects, using the Bruggeman correlation $\sigma_e^{eff} = \sigma_e \varepsilon_e^p$ with the Bruggeman coefficient p equal to 1.5.

(2) *Diffusive and electro migrative term* $\frac{\partial}{\partial x}\left(\frac{2RT\sigma_e^{eff}}{F}(1-t_{Li^+})\left(1+\frac{d(\ln f_\pm)}{d(\ln c_e)}\right)\left(\frac{\partial \ln c_e}{\partial x}\right)\right)$: This term accounts for the effects of ion diffusion (due to concentration gradients) and electromigration (due to Coulombic force acting on ions in an electric field) in the electrolyte. $2RT\sigma_e^{eff}/F$ represents the thermodynamic contribution to diffusion, dependent on temperature T, where R is the universal gas constant. $f_\pm$ is the mean molar activity coefficient which corrects for deviations from ideal behavior in electrolyte solutions due to ion interactions.

(3) *Electrochemical term* $A_s i$: due to the charge transfer reaction at the electrode-electrolyte interface.

The same boundary condition is applied at the electrode–current collector interfaces (i.e. $x = 0, x = d_{RL}$) assuming that all current i is transported through the solid phase. This leads to a of Neumann condition for the electrolyte, as shown in equation (13). Potential continuity is assumed across the electrodes and the separator. In summary, in Figure 3 all the boundary conditions are represented for the lithium-ion concentration within the electrolyte, and for the solid and electrolyte potential, without representing continuity conditions:

$$\left(\sigma_e^{eff}\frac{\partial\varphi_e}{\partial x}\right)_{x=0} = \left(\sigma_e^{eff}\frac{\partial\varphi_e}{\partial x}\right)_{x=d_{RL}} = 0 \tag{13}$$

As initial conditions, the electrolyte-phase potential φ_e is set to the equilibrium potential U_{eq} across the positive electrode thickness $d_{ele,p}$ and a reference electrolyte-phase zero-potential φ_e is assigned throughout the negative electrode thickness $d_{ele,n}$. In the separator region, the electrolyte-phase potential φ_e is assumed to transition linearly between the values in the adjacent electrodes.

2.1.3 Reaction kinetics equations. The electrochemical reaction kinetics at the interface between the solid electrode and the electrolyte follows the Butler–Volmer equation, describing the current density i as in the following equation:

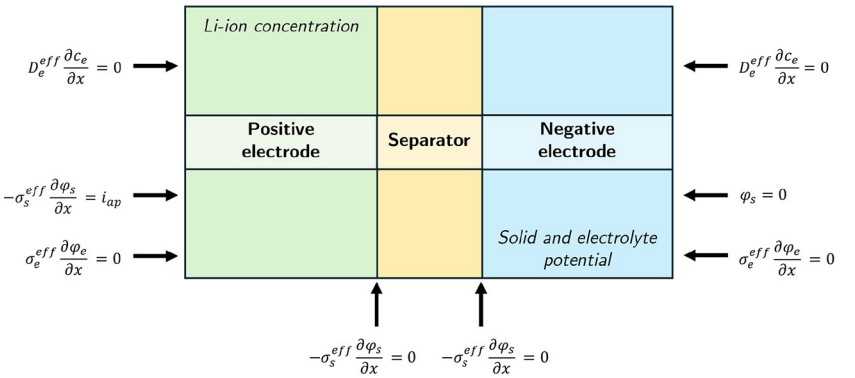

Figure 3. Schematic representation of the boundary conditions for the lithium-ion concentration within the electrolyte and for the solid and electrolyte potential

$$i = i_0\left(exp\left(\frac{\alpha_a F\eta}{RT}\right) - exp\left(-\frac{\alpha_c F\eta}{RT}\right)\right) \tag{14}$$

where i_0 represents the exchange current density, defined in equation (15), α_a and α_c denote the anodic and cathodic transfer coefficients, respectively, representing the directionality and balance of the overall reaction and η is the overpotential, which quantifies the deviation between the actual potential $\varphi_s - \varphi_e$ and the equilibrium voltage U_{eq}, defined in equation (16):

$$i_0 = Fk_0\left(\frac{c_e}{c_{e,ref}}\right)^{\alpha_a}\left(c_{s,max} - c_{s,R}\right)^{\alpha_a} c_{s,R}^{\alpha_c} \tag{15}$$

$$\eta = \varphi_s - \varphi_e - U_{eq} \tag{16}$$

where k_0 is the kinetic rate constant, $c_{e,ref}$ is the reference electrolyte concentration, equal to the initial electrolyte concentration $c_{e,0}c_{s,max}$ is the maximum concentration in the solid phase and $c_{s,R}$ indicates the solid phase concentration at the surface of the active particle, with $r = R_s$. The equilibrium voltage U_{eq} is a temperature-dependent value, approximated using a first-order Taylor series expansion:

$$U_{eq} = U_{eq,ref} + \frac{\partial U_{eq}}{\partial T}\left(T - T_{ref}\right) \tag{17}$$

Here, $U_{eq,ref}$ represents the reference equilibrium voltage, while T_{ref} denotes the corresponding reference temperature $\frac{\partial U_{eq}}{\partial T}$.

2.2 Thermal model

The computational domain of the battery thermal model is composed of a mandrel, a core and a case. The thermal behavior of the battery is modeled using cylindrical coordinates (r, θ, z). Due to the inherent symmetry of the cell, of the boundary conditions and of the thermal conductivity k along the angular direction, the coordinate θ is neglected, allowing the model to be simplified to a two-dimensional axisymmetric framework. This reduction, which considers only radial r and axial z coordinates, provides computational efficiency while

maintaining a high degree of accuracy compared to full three-dimensional simulations, as done in most thermal models coupled with P2D models (Alkhedher *et al.*, 2024). The dimensional reduction is justified by the uniform internal heat generation Q within the cylindrical cell core and a uniform thermal resistance along the angular direction θ. As a result, the external surface temperature T remains nearly uniform along the circumference, preventing localized hotspots that are commonly observed in pouch cells (Grandjean *et al.*, 2017; Dileep *et al.*, 2024). This symmetry simplifies the analysis while accurately capturing the dominant heat transfer mechanisms in the radial and axial directions. To simplify the computational domain and reduce computation time, the battery core is treated as a single homogeneous component that encapsulates all internal materials. The thermal conductivity k is considered anisotropic (Huang *et al.*, 2020), differing along the axial z and radial r directions. In particular, the axial thermal conductivity k_z is computed through equivalent thermal network theory of layers in parallel, assuming an axial heat flux, while the radial conductivity k_r follows a series layer's model, as detailed in Taheri *et al.* (2013) and shown in equations (18) and (19). The theory of equivalent thermal networks can be simplified by applying the formulations for flat sheets instead of cylinders, as the battery's radius of curvature (on the order of millimeters, starting from the mandrel radius r_{man}) is significantly larger than the thickness of its layers (in the order of micrometers). The density ρ and specific heat c are determined as volume- and mass-averaged values, respectively, as presented in equations (20) and (21). The battery reference length for the core thermal properties calculation, is the representative layer thickness d_{RL}, considering also the current collectors' thicknesses $d_{cc,p}$ and $d_{cc,n}$:

$$k_r = \frac{d_{RL} + d_{cc,p} + d_{cc,n}}{\sum_i^N \frac{d_i}{k_i}} \tag{18}$$

$$k_z = \frac{\sum_i^N k_i d_i}{d_{RL} + d_{cc,p} + d_{cc,n}} \tag{19}$$

$$\rho = \frac{\sum_i^N \rho_i d_i}{d_{RL} + d_{cc,p} + d_{cc,n}} \tag{20}$$

$$c = \frac{\sum_i^N c_i \rho_i d_i}{\sum_i^N \rho_i d_i} \tag{21}$$

Heat transfer within the battery follows the energy conservation equation:

$$\rho c \frac{\partial T}{\partial t} = k_r \left(\frac{\partial^2 T}{\partial r^2} + \frac{1}{r} \frac{\partial T}{\partial r} \right) + k_z \frac{\partial^2 T}{\partial z^2} + \dot{Q} \tag{22}$$

To model heat generation inside the core, the formulation proposed by Bernardi *et al.* (1985), Rao and Newman (1997) and Gu and Wang, (2000) is used. The total heat source in the one-dimensional domain Q_{1D}, is calculated along the x direction in the electrochemical model domain thickness, expressed in the following equations:

$$\dot{Q}_{1D} = \dot{Q}_{act} + \dot{Q}_{ohm} + \dot{Q}_{rev} \tag{23}$$

$$\dot{Q}_{act} = A_s i(\varphi_s - \varphi_e - U_{eq}) \tag{24}$$

$$\dot{Q}_{ohm} = \sigma_s^{eff}\left(\frac{\partial\varphi_s}{\partial x}\right)^2 + \sigma_e^{eff}\left(\frac{\partial\varphi_e}{\partial x}\right)^2 + \frac{2RT\sigma_e^{eff}}{F}(1 - t_{Li^+})\left(1 + \frac{d(ln\ f_{\pm})}{d(ln\ c_e)}\right)\left(\frac{\partial lnc_e}{\partial x}\right)\left(\frac{\partial\varphi_e}{\partial x}\right) \tag{25}$$

$$\dot{Q}_{rev} = A_s iT\frac{\partial U_{eq}}{\partial T} \tag{26}$$

These terms account for contributions from all internal components, including the electrodes, separator and current collectors, detailed in the following bullets:

- *Active polarization heat* $\dot{Q}_{act}$: Under open-circuit voltage conditions U_{eq}, the system remains in local equilibrium, with lithium-ion potentials in the electrolyte and electrode material matching. However, once current flows, restoring equilibrium requires energy dissipation, resulting in activation polarization heat $\dot{Q}_{act}$.
- *Ohmic heat* $\dot{Q}_{ohm}$: It arises from electronic and ionic resistances in different phases and is described by Joule's law, where the first term represents electronic ohmic losses in the solid phase, the second term accounts for ionic losses in the electrolyte and the third term describes ionic migration heating effects.
- *Reversible heat* $\dot{Q}_{rev}$: Based on the difference in energy levels between reactants and products, the electrochemical reaction either absorbs or releases heat to maintain thermodynamic equilibrium. The phenomenon is associated with entropy variations within the system, which can lead to either exothermic or endothermic reactions, depending on the entropy change. These reactions, in turn, influence the overall heat generation $\dot{Q}_{1D}$, either mitigating or exacerbating it. The effect is strongly dependent on the current density i, which changes sign during charge and discharge cycles, and on the SoC through the entropy coefficient $\partial U_{eq}/\partial T$ sign, that represents the temperature dependence of the equilibrium potential U_{eq} and is directly associated with entropy changes.

The heat generation calculated using equation (23) corresponds to the electrochemical model's computational domain, which does not account for the thicknesses of the current collectors $d_{cc,p}$ and $d_{cc,n}$. Consequently, the computed heat generation does not represent the correct volumetric heat generation. To incorporate the contribution of these components, the heat generation obtained from the P2D model, $\dot{Q}_{1D}$ must be scaled by a correction factor. This factor χ_{RL} is defined as the ratio between the representative layer thickness, d_{RL} and the total thickness, including the current collectors, given by the following equation:

$$\chi_{RL} = \frac{d_{RL}}{d_{RL} + d_{cc,p} + d_{cc,n}} \tag{27}$$

$$\dot{Q} = \dot{Q}_{1D} \cdot \chi_{RL} \tag{28}$$

Finally, the mandrel and the can are not heat-generating components.

Because ohmic drops along the current collectors are omitted as an assumption, the potential error introduced by this simplification is assessed. The omission of current collector ohmic losses can slightly underestimate the core heat generation. Since the heat generation in the current collectors is exclusively due to ohmic effects, it can be approximated as $\dot{Q}_{ohm,cc,j} = \frac{i^2}{\sigma_{cc}} \cdot \frac{d_{cc,i}}{d_{RL} + d_{cc,p} + d_{cc,n}}$ for a current collector j, positive or negative. Considering a current density $i = 50\ A/m^2$ and the relevant thicknesses d as reported in the Sections 3.1–3.2, respectively, and using electrical conductivities $\sigma_{cc,j}$ equal to 37.8 MS/m and 59.6 MS/m for aluminum (positive) and copper (negative) current collectors respectively (Goutam *et al.*, 2017), the resulting heat generation is $\dot{Q}_{ohm,cc,p} = 4.21 \times 10^{-6}$ W/m^3 and $\dot{Q}_{ohm,cc,n} = 1.87 \times 10^{-6}$ W/m^3, These values would add to the total heat generation $\dot{Q}$ predicted by the coupled electrochemical–thermal model, but are negligible in magnitude. In fact, they are several orders of magnitude lower than the heat generation obtained in our setup, which is on the order of 10^4 W/m^3. Therefore, the impact of this simplification is negligible and does not significantly affect the thermal predictions.

A Robin boundary condition is imposed along the external surface of the battery (i.e. the case), characterized by a fixed convective heat transfer coefficient h and an ambient temperature T_{amb}, while temperature continuity is ensured across the different regions. As the initial condition, the entire computational domain is uniformly set to the ambient temperature T_{amb}. A schematic representation of the computational domain, the components and of the applied boundary condition is depicted in Figure 4:

$$\dot{q}_{conv} \cdot n = -(k\nabla T) \cdot n = h(T - T_{amb}) \tag{29}$$

Since the thermal model depends on several electrochemical parameters, and while key properties like the electrolyte diffusion coefficient D_e, the electrolyte conductivity σ_e, the mean molar activity coefficient $f_\pm$ and the potential equilibrium U_{eq} exhibit temperature dependence, coupling the thermal and electrochemical models is essential for accuracy. To achieve this, the average core surface temperature $T_{co,av}$ computed from the thermal model at each time step, is used to update the electrochemical model, as described in equations (30) and (31). D_e, σ_e and $f_\pm$ temperature-dependency are calculated through Arrhenius equation [equation (31)], while the potential equilibrium U_{eq} is calculated through equation (17):

$$T_{co,av} = \frac{1}{A_{co}} \int_{A_{co}} T(r, z) dA \tag{30}$$

$$p = p_{ref} exp\left[\frac{E_{act,p}}{R}\left(\frac{1}{T_{ref}} - \frac{1}{T_{co,av}}\right)\right] \qquad p = D_e,\ \ \sigma_e,\ \ f_\pm \tag{31}$$

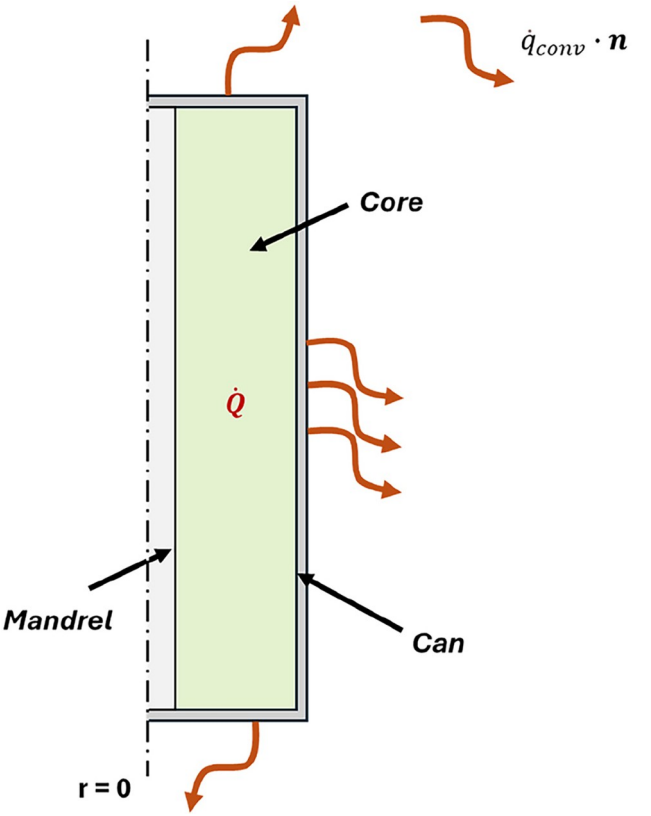

Figure 4. Schematic representation of thermal model computational domain, of the components and of the applied boundary condition

where A_{co} is the core area in the 2D domain, p is the temperature-dependent parameter and $E_{act,p}$ and represents the activation energy associated with the parameter p, governing its sensitivity to temperature variation. The updated electrochemical parameters are then fed back into the thermal model to determine heat generation within the core, introducing additional non-linearity into the system, as depicted in the flowchart in Figure 5. This iterative coupling ensures real-time updates of temperature-dependent parameters, maintaining consistency between the thermal and electrochemical models.

2.3 Phase change material model

When simulating phase change materials, three distinct regions can be identified: a solid phase, a liquid phase and an intermediate mushy region where both phases coexist. In the numerical model, the heat transfer within the liquid phase is assumed to occur primarily through conduction, with natural convection effects being disregarded. This assumption is justified by the small thickness of the PCM layer in the given application, where buoyancy-driven flow can be considered negligible. To validate this simplification, a scaling analysis was performed based on the Rayleigh number:

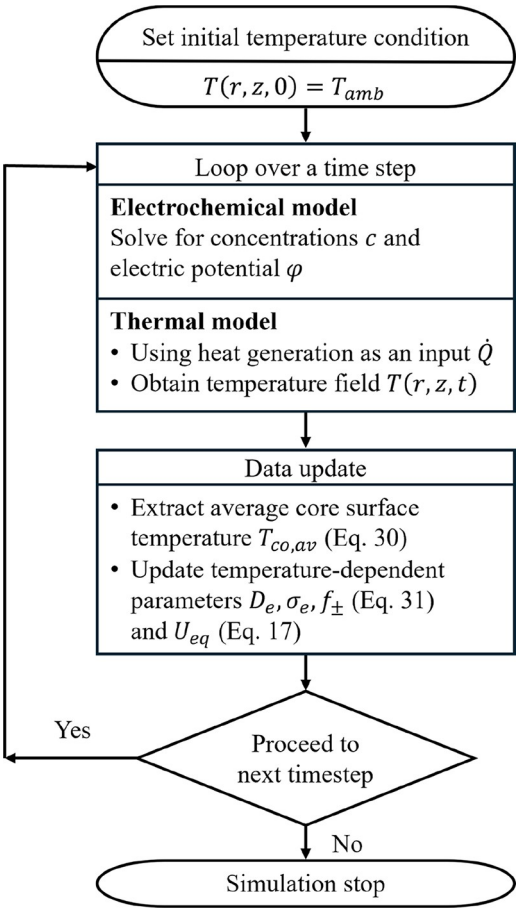

Figure 5. Flowchart of the way of coupling between the P2D electrochemical model and the 2D thermal model

$$Ra = \frac{g\beta\Delta T L^3}{\nu\alpha} \tag{32}$$

where, g gravity acceleration, β is the thermal expansion coefficient, using a standard value equal to 10^{-3} for molten salts that will be used in this work, ΔT is the temperature difference, L is the characteristic length, ν is the kinematic viscosity and $\alpha = k/\rho c$ is the thermal diffusivity. Two characteristic Rayleigh numbers were calculated using different length and temperature scales, representative of each geometry:

- *Internal PCM:* The characteristic length was taken as the mandrel radius r_{man}, as the heat flow direction is along the radius, and a temperature difference of $\Delta T = 1°C$ was assumed, based on the near-isothermal behavior of the small mandrel region (from center to outer PCM interface).

- *External PCM layer:* The characteristic length was taken as the actual PCM thickness d_{PCM} used in the external configuration (as discussed later, in Section 3.2). For the temperature gradient, a maximum temperature difference $\Delta T = 30^{\circ}\text{C}$ was considered, corresponding to a worst-case battery surface temperature versus ambient, with the maximum battery operating temperature equal to 50°C (Rodrigues *et al.*, 2017; Jiang *et al.*, 2020) and the ambient temperature equal to $T_{amb} = 20^{\circ}\text{C}$.

For the internal PCM configuration, the Rayleigh number obtained is equal to 86, while for the external configuration, the Rayleigh number is even smaller. Given that these values are significantly low to the typical critical values (≈1,000) for considering natural convection phenomenon and considering the radial orientation of the heat flow (orthogonal to gravity), the simplification of neglecting natural convection is justified.

In addition, the following assumptions are considered:

- The PCM is treated as a homogeneous material with isotropic characteristics.
- Volume variations during phase transition are negligible, and the formation of air gaps due to expansion or contraction is disregarded.

In the absence of natural convection, the governing energy conservation equation for the PCM, formulated using an enthalpy-based method to account for latent heat effects (Fragnito *et al.*, 2022), reduces to:

$$\rho c\left(\frac{\partial T}{\partial t}\right) = k_r\left(\frac{\partial^2 T}{\partial r^2} + \frac{1}{r}\frac{\partial T}{\partial r}\right) + k_z\frac{\partial^2 T}{\partial z^2} + S_h \tag{33}$$

where the term S_h is used to model the release or absorption of latent heat during melting or solidification, expressed as:

$$S_h = -\rho H_l \frac{\partial \psi}{\partial T} \tag{34}$$

where H_l is the latent heat of fusion, and ψ is a dimensionless variable that represents the fraction of liquid phase, calculated as a function of temperature T:

$$\psi(T) = \frac{V_{liq}}{V_{PCM}} = \begin{cases} 0 \;\; if \;\; T \le T_{sol} \\ \dfrac{T - T_{sol}}{T_l - T_{sol}} \;\; if \;\; T_{sol} < T < T_l \\ 1 \;\; if \;\; T \ge T_l \end{cases} \tag{35}$$

V_l and V_{PCM} are the liquid fraction volume and the entire PCM volume, respectively, T_{sol} is the solidification temperature limit and T_l is the melting temperature limit. Continuity in the first derivative is maintained at the interfaces between the fully solid phase and the phase transition region, as well as between the fully liquid phase and the phase transition region. This prevents abrupt variations in the temperature T and avoids discontinuities.

The material properties are defined as temperature-dependent functions, expressed in terms of the liquid fraction $\psi(T)$, allowing for a continuous and thermodynamically consistent transition between solid and liquid phases. This approach is necessary because

thermophysical properties such as density ρ, thermal conductivity k and specific heat c undergo significant variation during phase change and a smooth interpolation based on $\psi(T)$, ensures realistic representation of the transient melting behavior:

$$Y = Y_{sol}\left(1 - \psi(T)\right) + Y_l\psi(T) \qquad Y = \rho,\, c,\, k \tag{36}$$

3. Materials and configurations analyzed

In this section a detailed description is provided of the electrical, chemical and thermal properties of the analyzed battery, as well as the thermal characteristics of the phase change material used in the study. In addition, the setup used for validation with the results from (O'Regan *et al.*, 2022; Cianciullo *et al.*, 2022) is outlined and are discussed the different configurations designed to assess the benefits of PCM integration – internally within a hollow mandrel, externally around the battery and in a combined internal–external arrangement. Finally, a study on the optimal PCM thickness in the external and internal–external configuration is performed to minimize the overall battery pack volume while ensuring that the temperature remains within safe operating limits.

3.1 Battery and phase change material case study

The battery analyzed is a LCO 18650 cylindrical battery with a capacity C of 3.5 Ah and a nominal voltage U_{nom} = 4.2 V. The dimensions that are necessary for both the electrochemical and the thermal model are depicted in Figure 6(a) and (b), respectively, while the battery electrochemical–thermal properties, and the phase change material thermal properties are detailed in Tables 1–3. In particular, the phase change material used is the sodium thiosulfate pentahydrate (STP), a molten salt with key thermal parameters detailed in references (Moynihan, 1966; Hadjieva *et al.*, 2000; Landini *et al.*, 2019). The selected PCM was chosen for its favorable thermal properties for battery applications. It exhibits a melting temperature range (40–48°C), which is close to the maximum limit T_{lim} = 50°C recommended by manufacturers (Jiang *et al.*, 2020), high latent heat (210 kJ/kg), chemical stability and non-flammability. These features make it a suitable candidate for compact passive thermal protection systems in lithium-ion cells. As the battery temperature reaches

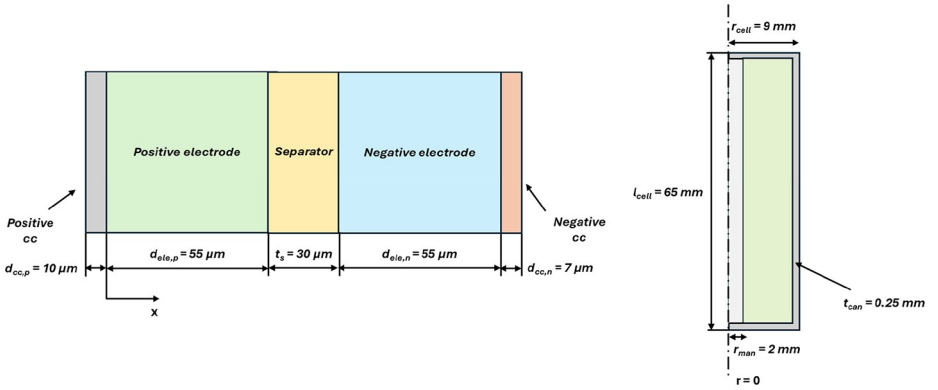

Figure 6. Battery dimensions for the electrochemical model (a) and the thermal model (b)

Table 1. Thermal properties of each battery component

Component	Material	Thermal conductivity k [W/(mK)]	Density ρ [kg/m^3]	Heat capacity c [J/(kgK)]
Positive electrode	Graphite Li_xC_6	1.04	1,347	1,437
Negative electrode	$LiCoO_2$	1.48	2,500	700
Separator	Polyethylene	0.34	1,009	1,978
Positive current collector	Aluminum	170	2,770	875
Negative current collector	Copper	298	8,933	385
Mandrel	Nylon	0.26	7,850	475
Can	Steel	44.5	1,150	1,700

Table 2. Electrical and chemical battery properties

Symbol	Description	Value	
t_{Li^+}	Electrolyte ionic current fraction by lithium ions [/]	0.36	
	Anode	Cathode	
R_s	Solid phase particle radius [μm]	12.50	8.00
D_s	Solid phase diffusion coefficient [m^2/s]	3.90×10^{-14}	1.00×10^{-13}
$c_{s,0}$	Initial concentration in the solid phase [mol/m^3]	7,917	16,002
$c_{e,0}$	Initial concentration in the electrolyte phase* [mol/m^3]	2,000	2,000
$c_{s,max}$	Maximum concentration in the solid phase [mol/m^3]	26,390	22,860
ε_s	Volume fraction in the solid phase [/]	0.471	0.297
ε_e	Volume fraction in the electrolyte phase [/]	0.357	0.444
φ_s	Solid phase electrical conductivity [S/m]	0.113	100
α_i	Charge transfer coefficient [/]	0.5	0.5
k_0	Kinetic rate constant [m/s]	2.00×10^{-11}	3.90×10^{-11}

Note(s): *For the separator $c_{e,0}$ is equal to 2,000 [mol/m^3]

Table 3. Sodium thiosulphate pentahydrate ($Na_2S_2O_3 \cdot 5H_2O$) thermal properties

Symbol	Description	Value
$T_s - T_l$	Melting range [°C]	40 − 48
H_l	Latent heat of fusion [kJ/kg]	210
ρ_s	Solid phase density [kg/m^3]	1,720
ρ_l	Liquid phase density [kg/m^3]	1,666
c_s	Solid phase heat capacity [kJ/kgK]	1.46
c_l	Liquid phase heat capacity [kJ/kgK]	2.39
k_s	Solid phase thermal conductivity [kJ/mK]	0.76
k_l	Liquid phase thermal conductivity [kJ/mK]	0.38
ν	Kinematic viscosity* [m^2/s]	1.14×10^{-5}

Note(s): *Obtained by dividing the dynamic viscosity μ, from Moynihan (1966) with the liquid density from Landini *et al.*, (2019)

the phase change region of the PCM, the latent heat H_l acts as a thermal buffer by maintaining the PCM temperature nearly constant. During this period, the absorbed latent heat temporarily stores the energy dissipated by the battery, thereby slowing the rise in cell temperature $\partial T/\partial t$ and stabilizing the thermal behavior of the system. This extended thermal regulation provides a longer response time to implement protective measures, reducing cell degradation and ensuring safety for individuals in proximity to the battery. Molten salts were chosen over paraffins because paraffins are highly flammable and may pose safety hazards near batteries.

The thermal properties of each core battery component are specified, taken from Cianciullo *et al.* (2022), and these have been used in the calculation of the core's overall thermal properties. The electrochemical parameters are derived from (Melcher *et al.*, 2016), where the electrolyte is $LiPF_6$ in 1:1 EC:DEC, with the electrolyte phase diffusion coefficient D_e, phase conductivity φ_e, mean molar activity coefficient $f_\pm$ and the entropy coefficient $\frac{\partial U_{eq}}{\partial T}$ of both positive and negative electrodes have been evaluated through the COMSOL Multiphysics material library of the battery components, listed in Table 1. These properties have been used both for the numerical comparison with (Cianciullo *et al.*, 2022) and for the simulations presented in this study (Table 1 to 3).

3.2 Validation setup, different phase change material configurations

To ensure consistency and reliability of the proposed coupled electrochemical–thermal model, a validation was performed against the experimental results provided by (O'Regan *et al.*, 2022). The simulation replicates the same operating conditions adopted in their study: constant 1C discharge (where 1C represents the applied current required to fully discharge the battery within one hour), ambient temperature T_{amb} = 25°C (considered also as initial temperature) and a convective heat transfer coefficient h = 15 W/m^{2}K. Following the full discharge phase, the model also simulates the subsequent rest period up to 10,000 s, allowing for a direct comparison of the cell's thermal relaxation behavior. The electrochemical and thermal properties of the battery used in this validation case are set equal to those reported in (O'Regan *et al.*, 2022), to ensure full compatibility with the experimental reference. The comparison focuses on the evolution of the average surface temperature $T_{sur,avg}$ as the experimental studies do not specify the exact location of the thermocouple on the cell surface. Therefore, the simulated value is taken as the average temperature along the cylindrical surface of the cell. Given the nearly isothermal behavior of the surface – supported by the relatively high axial thermal conductivity k_z – this approximation introduces minimal error and remains representative of the measured experimental quantity. Then, numerical results for the average battery temperature are compared with those reported in (Cianciullo *et al.*, 2022), which validated their model through the thermal runaway ignition time t_{TR} – the time required for a battery to reach the initiation of thermal runaway – with a previously validated study using the P2D model (Melcher *et al.*, 2016). A charge/discharge cycle is simulated, using battery characteristics reported in Section 3.1, lasting 500 s per full cycle, for a time period t = 7,000 s, beginning with the charging phase at a current density i of ±80A/m^2, as depicted in Figure 7. The analysis considers two different convective heat transfer coefficients, h, set to 4 W/m^{2}K and 6 W/m^{2}K and an ambient temperature T_{amb} of 20°C, corresponding to a natural convection with air. Assuming an electrode surface area of 0.1 m^2, as determined in (Saw *et al.*, 2013), the current density at 1C is 35A/m^2. In this study, the comparison is conducted at 2.3C.

The different configurations analyzed are a function of the PCM position: internally within a hollow mandrel, externally around the battery can and together in

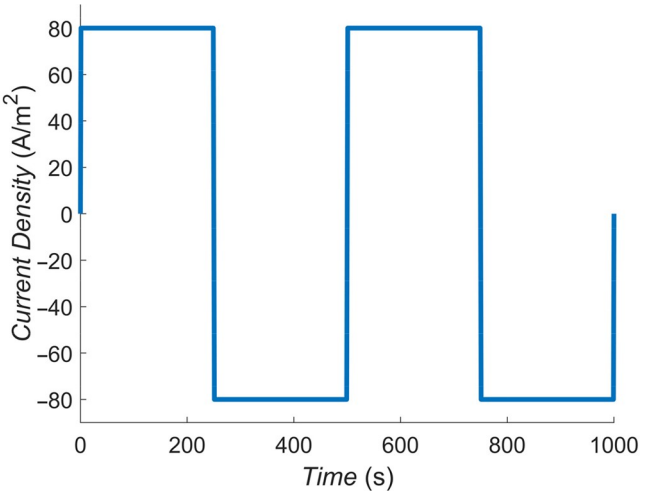

Figure 7. Charge/discharge cycle used with for the comparison with the model from (Cianciullo *et al*., 2022)

an internal/external configuration, as shown in Figure 8. The volume of the internal PCM is equal to that of the mandrel, under the assumption that the enclosing container prevents any PCM leakage into the battery, thereby avoiding direct contact. The containers for both internal and external PCM are not explicitly modeled, as their thickness – on the order of a tenth of a millimeter – make their thermal influence negligible. The comparison between internal and external PCM configurations is conducted for an equivalent PCM volume, leading to an external PCM layer thickness d of 0.22 mm. This assumption allows for an assessment of the potential advantages of an internal PCM relative to an external one, acknowledging that such a thickness is minimal in the context of a battery pack. However, the integration of an internal PCM would not contribute to an increase in the outer casing thickness. When scaled across multiple cells within an industrial battery pack, this distinction could be significant in terms of overall footprint. For fair comparison across configurations (internal, external, internal/external), volume constraints were applied where necessary, ensuring that improvements in thermal performance are not merely due to additional PCM volume, which would naturally lead to better thermal management, but rather to more efficient spatial placement. At the interface between the battery surface and the PCM domain (internal, external or combined), temperature continuity is ensured. This condition accounts for heat transfer between the cell and the adjacent PCM material, effectively coupling the thermal behavior of both regions. Then, for the external PCM, the same Robin boundary condition is applied as for the reference case. The analysis focuses on the average temperature T plot by each configuration, the time required for the battery to reach the temperature limit T_{lim} of 50°C and on the volume averaged PCM melting fraction ψ, aiming to determine which configuration offers superior thermal management while optimizing battery efficiency and spatial constraints for potential battery pack applications. To compare the time to reach T_{lim}, a time improvement percentage is defined as in equation (37):

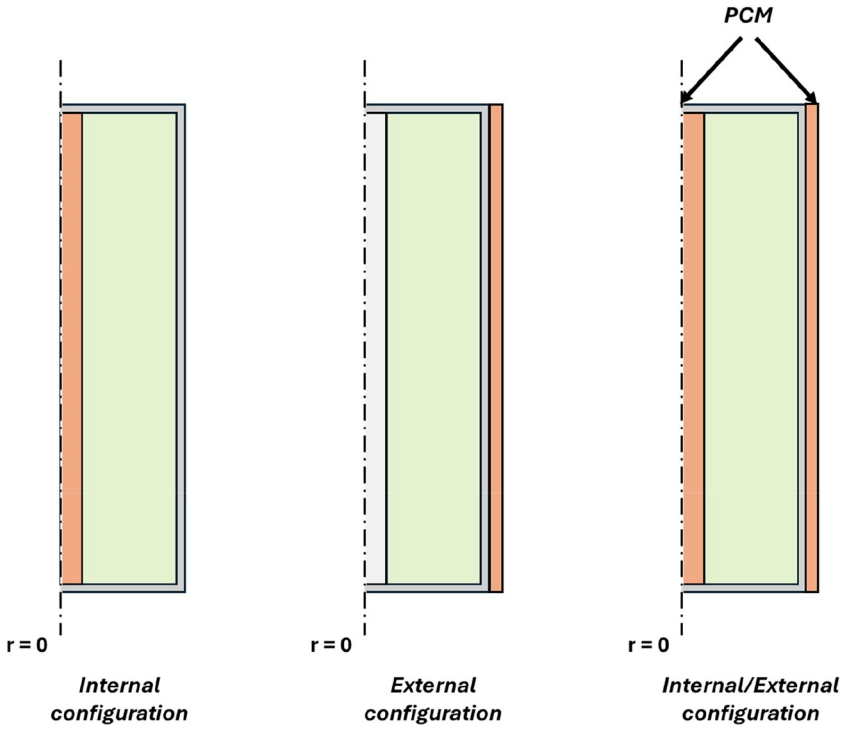

Figure 8. Three phase change material (PCM) configurations for the battery, where PCM material (orange) is located in the hollow center mandrel space and/or wrapped as a cylindrical shell around the battery exterior

$$I_t = \frac{t_{stop} - t_{stop,\,ref}}{t_{stop,\,ref}} \tag{37}$$

where t_{stop} is the time when the maximum temperature T_{max} reaches the temperature limit T_{lim} for the configuration under analysis, while $t_{stop,\,ref}$ represents the corresponding time t_{stop} for the compared reference configuration. In this study, the reference configuration represents the single battery without PCM. The studies have been done with the same pulse discharge/charge cycle from the comparison with the work of (Cianciullo *et al.*, 2022) for a time t of 7,000 s, but a different current density i of $\pm 50 A/m^2$ (i.e. 1.5C), that correspond to a standard current for industrial applications. The corresponding boundary conditions used are an ambient temperature T_{amb} of 20°C, and two different heat transfer coefficients $h = 8$ W/m^2K and 10 W/m^2K, corresponding to two different natural convection conditions in air.

In addition, a parametric analysis that varies the external PCM thickness t_{PCM}, was conducted to determine the optimal thickness t_{opt} required to prevent the battery from exceeding the temperature limit $T_{lim} = 50$°C and the operational temperature limit $T_{lim,\,op}$, set at 45°C. This threshold was set as a safety measure that battery customers could apply for designing their battery packs, to prevent the battery from reaching the temperature limit T_{lim}, to mitigate the risk of potential damage and ensure safer operating conditions. The

simulations have been performed with an external ambient temperature $T_{amb} = 20°C$, and a heat transfer coefficient $h = 10\ W/m^2K$, for a time t of 7,000 s, making also a grid consistence analysis to assure the validity of the results. The test was performed on the most challenging configuration, with a 2 mm PCM external layer, in the internal and external configuration, making it the most sensitive to discretization errors. Based on the outcome of this test, grid independence is assumed to hold for all other configurations as well, including those with the mandrel and with reduced PCM thicknesses.

Since the simulation time is extended, with this heat transfer coefficient h, the configuration goes to a thermal equilibrium after a certain period, and for this reason a trend of the maximum temperature T_{max} (i.e. the final temperature, at $t = 7,000$ s) as a function of external PCM thickness t_{PCM} in both external and internal/external configuration is presented. The objective is to assess the spatial benefits of incorporating an internal PCM, optimizing the battery pack design by reducing its footprint, quantifying a volume saving percentage, expressed in equation (38). The parametric analysis focuses on the variation of PCM thickness, as this geometric parameter directly impacts the spatial footprint of the battery unit. This study aims to determine the minimum external PCM thickness in the internal/external configuration needed to keep the cell temperature within safe limits, and to compare it with the external-only configuration yielding the same maximum temperature T_{max}:

$$V_{sav} = \frac{{r_{ref}}^2 - r^2}{{r_{ref}}^2} \tag{38}$$

where ${r_{ref}}^2$ is the total radius (battery+PCM) of the reference system to be compared.

4. Results and discussion

The validation of the model with the results of O'Regan *et al.* (2022) and Cianciullo *et al.* (2022) are presented in Figures 9–10 terms of the average surface temperature $T_{sur,avg}$ and of the maximum battery temperature T_{max}, respectively, for different convective heat transfer coefficients h. For the experimental results of O'Regan *et al.*, the temperature trend is consistent during both the discharge and relaxation phases, as shown in Figure 9. The only discrepancy is that the experimental battery temperature drops below 25°C, indicated as the ambient temperature T_{amb}, whereas in the simulation it does not, since 25°C is assumed as the minimum possible temperature. For the results of Cianciullo *et al.* (2022), the temperature trends indicate significantly high values in both configurations (Figure 10), suggesting that the thermal runaway mechanism is likely to be triggered. The similarity of the temperature curves T confirms that the model accurately represents the typical thermal behavior of a battery. The observed fluctuating temperature trend T results from the alternating charge and discharge phases, which cause variations in current density i and, consequently, in reversible heat generation Q_{rev}. Since the entropy coefficient $\partial U_{eq}/\partial T$ is predominantly positive, the system experiences a lower temperature rise $\partial T/\partial t$ during discharging, as the entropy-driven heat contribution partially offsets the heat generated during the process As a result, the total heat generation is partially offset, leading to a reduced temperature increase $\partial T/\partial t$ during discharge. To better quantify the model's accuracy, both the root mean square (RMS) error and the maximum error were evaluated, as shown in Table 4. For the case by O'Regan *et al.* (2022) a RMS error of 1.01°C and a maximum error of 2.50°C were observed. Although experimental uncertainty values are not explicitly reported in the cited study, a typical thermocouple accuracy of ± 1°C is assumed, consistent with standard practices of thermocouples. For the comparison against (Cianciullo

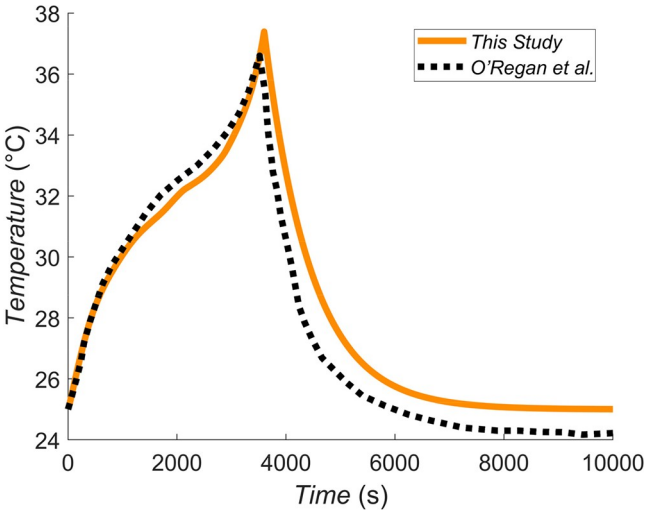

Figure 9. Validation with (O'Regan *et al.*, 2022) in terms of the average surface temperature $T_{sur,avg}$ for a convective heat transfer coefficient $h = 15\ \mathrm{W/m^2K}$

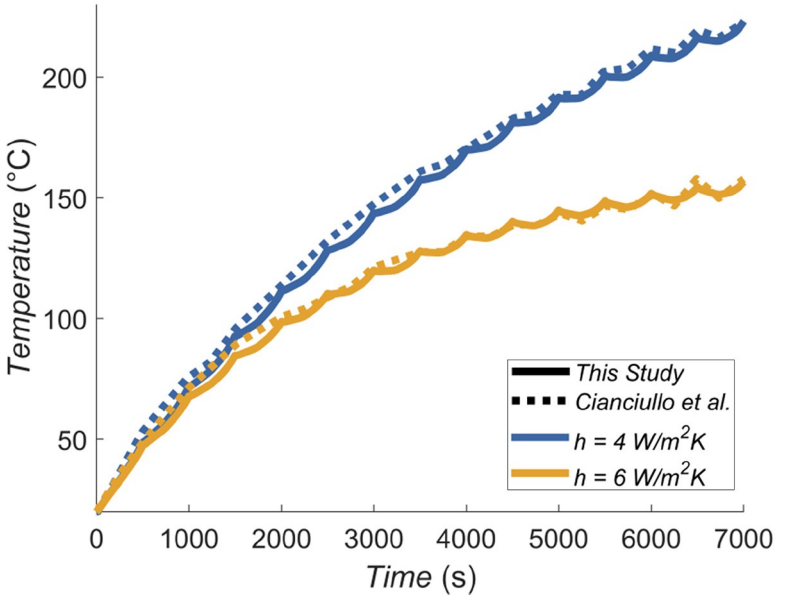

Figure 10. Results comparison with (Cianciullo *et al.*, 2022) in terms of the maximum battery temperature T_{max} for two different convective heat transfer coefficients $h = 4\ \mathrm{W/m^2K}$ and $h = 6\ \mathrm{W/m^2K}$

Table 4. Root mean square error and maximum error values for the average surface temperature $T_{sur,avg}$ for the validation with O'Regan *et al.*, (2022) and of the maximum temperature T_{max} for the comparison with Cianciullo *et al.*, (2022)

Study	RMS error [°C]	Maximum error [°C]	Temperature range [°C]
O'Regan *et al.*, 2022; $h = 15\ W/m^2$	1.01	2.50	25.0 – 36.6
Cianciullo *et al.*, 2022; $h = 4\ W/m^2$	2.02	4.01	20.0 – 223.0
Cianciullo *et al.*, 2022; $h = 6$?/,?-2. $h = 6\ W/m^2$	1.15	3.93	20.0 – 157.8

et al., 2022), the RMS error was 1.15°C for $h = 4\ \mathrm{W/m^2K}$ and 2.02°C for $h = 6\ \mathrm{W/m^2K}$, with corresponding maximum errors of 3.93°C and 4.01°C. Although these error values may appear relatively high, they occur over very wide temperature ranges (up to 223°C), which naturally amplifies the absolute deviation. This trend highlights how the error magnitude increases with the thermal excursion yet remains acceptable relative to the simulated and measured temperature scales. Remaining discrepancies may result from several factors, including uncertainties in material properties and modeling assumptions. Key thermophysical and electrochemical parameters – such as thermal conductivity k, specific heat capacity c, density ρ and electrical conductivity σ, – may vary with temperature T, yet are typically treated as constant in numerical models. In addition, electrochemical properties such as the entropy coefficient $\partial U_{eq}/\partial T$ and ionic diffusivity σ_e are sensitive to the SoC, aging effects and electrode microstructure, which may deviate from literature values or experimental results. These deviations, combined with the simplification of a uniform convective boundary conditions may contribute to the residual error observed between simulation and experiment. Nevertheless, considering all these factors and the overall agreement with multiple data sets, the model can be considered validated for the intended thermal analysis applications (Table 4).

To verify mesh independence, a sensitivity analysis was performed for the internal/external PCM configuration, using an external PCM thickness d of 2 mm The monitored variable was the temperature at the mid-height along the battery axis, in the region originally occupied by the mandrel, now filled with PCM ($T_{man,max}$), which corresponds to the thermal hotspot in this configuration. The temperature was evaluated at the end of the charge/discharge cycle, when the accumulated heat is maximal. As shown in Figure 11, mesh refinement leads to a monotonic decrease in $T_{man,max}$. The goal of the mesh refinement study was to achieve convergence of $T_{man,max}$ up to the second decimal place. As shown in Figure 11, the difference between the two finest meshes (30,260 and 62,697 elements) is zero at this precision, indicating no variation in the second decimal digit. Since further refinement does not affect the result at the target precision, the mesh with 30,260 elements is selected. This choice balances numerical accuracy with computational efficiency and confirms that the solution is mesh-independent at the chosen precision. This mesh is therefore used for all subsequent simulations.

The maximum temperature evolution over time is analyzed for the three configurations under investigation: internal, external and combined internal/external PCM, along with a reference case featuring a single battery configuration without PCM. The results are presented for two convective heat transfer coefficients $h = 8\ \mathrm{W/m^2K}$ and $h = 10\ \mathrm{W/m^2K}$ in Figures 12(a) and 13(a). As expected, the reference configuration exhibits the highest temperatures, as it does not benefit from the latent heat absorption associated with the PCM phase transition. Conversely, the internal/external configuration yields the best thermal

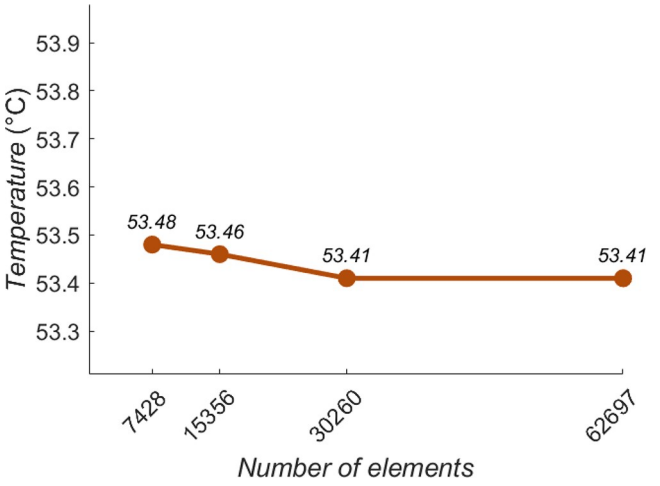

Figure 11. Results comparison with (Cianciullo *et al.*, 2022) in terms of the maximum battery temperature T_{max} for two different convective heat transfer coefficients $h = 4\ \mathrm{W/m^2K}$ and $h = 6\ \mathrm{W/m^2K}$

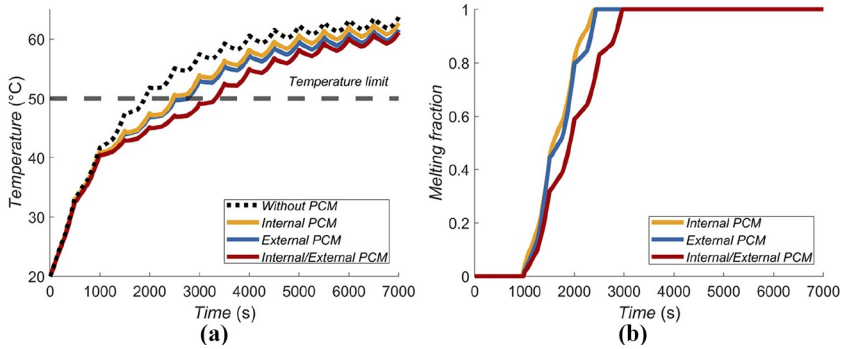

Figure 12. Maximum battery temperature T_{max} (a) and PCM melting fraction ψ (b) during time t for a heat transfer coefficient $h = 8\ \mathrm{W/m^2K}$

performance, as it effectively uses twice the PCM volume compared to the other two configurations. The internal and external PCM configurations produce similar temperature trends, with the internal PCM reaching the temperature limit T_{lim} slightly earlier. The superior performance of the internal/external PCM configuration can be explained by a more favorable redistribution of latent heat buffering. While the internal PCM offers high thermal contact with the core, it lacks direct exposure to the ambient, leading to slower heat rejection. On the contrary, the external PCM benefits from enhanced convective cooling due to its position but responds later to temperature spikes generated at the battery core. By combining the two, the system achieves a more balanced thermal gradient, which slows down the propagation of heat from the center and prolongs the phase change process. This effect is particularly visible in the time-dependent melting fraction curve, in Figures 12(b) and 13(b).

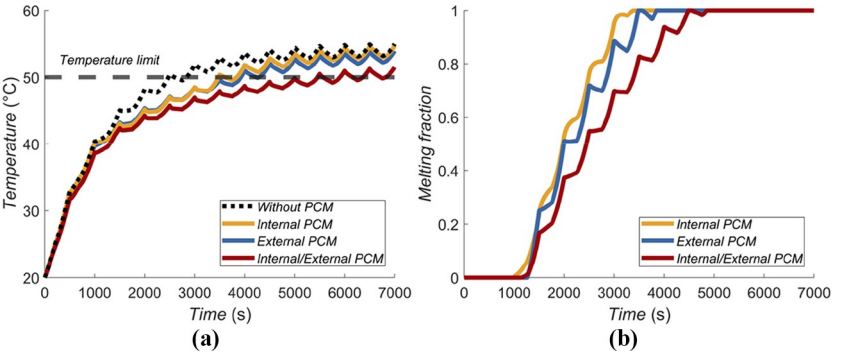

Figure 13. Maximum battery temperature T_{max} (a) and PCM melting fraction ψ (b) during time t for a heat transfer coefficient $h = 10\ \mathrm{W/m^2K}$

The rate at which the PCM transitions varies $\partial\psi/\partial t$ depends on the applied charge or discharge, as these influence heat generation Q through the reversible heat effects $\dot{Q}_{rev}$, which are positive during charge and negative during discharge, thereby reducing or increasing the overall heat generation Q. As soon as the phase transition begins, approximately at 1,000 s, the temperature rise $\partial T/\partial t$ significantly decreases compared to the case without PCM. This effect is due to the latent heat absorption H_l, which creates a temperature plateau as the system approaches the limit temperature region T_{lim}. In all cases analyzed, the temperature limit T_{lim} is exceeded. Although the absolute reduction in peak temperature is moderate under the given electrochemical and thermal conditions, the PCM demonstrates its effectiveness by significantly extending the safe operating time of the battery system. This behavior is expected in systems without strong active cooling, where the PCM acts primarily as a thermal buffer. Through latent heat absorption, it delays the onset of critical temperatures rather than drastically reducing the peak temperature. Therefore, the thermal benefit of PCM is more meaningfully evaluated in terms of time gained before reaching the limit temperature T_{lim}, rather than the magnitude of temperature drop itself. This is clearly reflected in the time improvement I_t to reach the limit temperature t_{stop}. The external PCM, compared to the internal configurations, performs marginally better in terms of thermal management efficiency. As reported in Table 5, for $h = 8\mathrm{W/m^2K}$, the time improvement I_t in reaching the limit temperature is 32.8% for the internal PCM, 48.2% for the external PCM and 78.8% for the internal/external PCM configuration, compared to the reference case. Similarly, Table 6 shows that for $h = 10\mathrm{W/m^2K}$, the time improvements I_t increase to 40.5%, 58.6% and 120.5%, respectively. This trend confirms that, in all configurations, a higher convective heat transfer coefficient delays the attainment of the limit temperature T_{lim} is reached later for higher convective heat transfer coefficients h across all configurations. This is because increasing h enhances heat dissipation to the surroundings, particularly in configurations where the PCM is placed on the outer side, which in turn slows down the phase transition rate $\partial\psi/\partial t$. As a result, the PCM remains in the phase change regime for a longer period, thereby providing more effective thermal buffering. Consequently, the thermal performance is improved for $h = 10\ \mathrm{W/m^2K}$ as the prolonged phase transition extends the PCM's temperature-regulating capacity. In summary, these results confirm the higher effectiveness of the internal/external arrangement, which benefits both from increased PCM volume and synergistic heat dissipation dynamics. In addition, the duration of the phase transition is longer in the internal–external PCM configuration than in

Table 5. Time improvement I_t to reach the limit temperature t_{stop} of the three configurations analyzed compared to the configuration without PCM for a heat transfer coefficient $h = 8\ W/m^2K$

Configuration	Time improvement I_t [%]
Internal	32.8
External	48.2
Internal/External	78.8

Table 6. Time improvement I_t to reach the limit temperature t_{stop} of the three configurations analyzed compared to the configuration without PCM for a heat transfer coefficient $h = 10\ \mathrm{W/m^2K}$

Configuration	Time improvement I_t [%]
Internal	40.5
External	58.6
Internal/external	120.5

the other cases, as it benefits from a greater PCM volume. However, if the objective is space optimization for battery packs, the internal PCM configuration provides comparable thermal performance while improving spatial integration, obtaining a volume saving V_s of 4.7% compared to the PCM external configuration.

Finally, the results of the parametric analysis on the maximum temperature T_{max} – which coincides with the final simulation temperature – are presented. As shown in Figure 14(a), when the convective heat transfer coefficient h is 10 $\mathrm{W/m^2K}$, the system nearly reaches thermal equilibrium under the applied electrochemical and thermal conditions. Therefore, the analyzed maximum temperature represents a plausible estimate of the system's potential

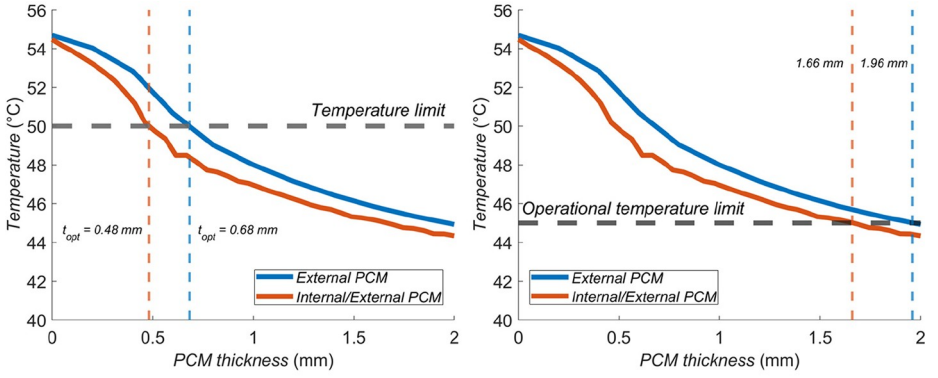

Figure 14. Maximum battery temperature T_{max} as a function of PCM external thickness, optimal PCM thickness t_{opt} calculation considering the temperature limit T_{lim} = 50°C (a) and the operational temperature limit $T_{lim,op} = 45°C$ (b)

peak temperature under these conditions. The maximum temperature T_{max} trend is examined as a function of PCM thickness t_{PCM} (with zero thickness indicating the absence of external PCM). As shown in Figure 14, considering the temperature limit T_{lim}, an optimal PCM thickness t_{opt} of 0.48 mm is identified for the internal/external configuration, while 0.68 mm is required for the external-only configuration. This corresponds to a 4.1% reduction in volume saving V_{sav}. Considering the operational temperature limit $T_{lim,op}$ in Figure 14(b), the optimal PCM thickness t_{opt} increases to 1.66 for the internal/external configuration and 1.96 for the external configuration, corresponding to a 5.4% volume saving V_s. This result highlights that incorporating PCM internally reduces the external space requirements within a battery pack, especially if one wants to prevent it from arriving near the temperature limit T_{lim}. This finding is particularly relevant for automotive battery packs, where size optimization is critical due to space constraints in vehicle design. By integrating PCM internally, the thermal management system can achieve comparable performance while minimizing the battery pack footprint.

5. Conclusions

In this work, a detailed electrochemical–thermal model of a cylindrical 18650 Li-ion cell was developed to assess the performance of three passive thermal management strategies using STP as PCM: internal PCM (placed in the mandrel), external PCM (wrapped around the cell) and a combined internal/external configuration. The results highlight the advantages of integrating PCM internally within the battery, both in terms of thermal regulation and space optimization.

The main findings of this study are as follows:

- The combined internal/external PCM configuration provided the best thermal performance, with a time improvement I_t of to 120.5% in delaying the temperature rise compared to the reference case without PCM, with a heat transfer coefficient $h = 10\ \mathrm{W/m^2K}$.
- While the internal and external configurations exhibited similar peak temperatures, the external PCM performed slightly better thermally due to more effective convective heat rejection.
- The internal PCM, despite having slightly lower thermal efficiency, enabled significant space optimization, offering a 4.7% volume reduction compared to external-only PCM.
- A parametric analysis of PCM thickness identified the optimal PCM layer for both external and hybrid configurations. The internal/external layout required 5.4% less PCM volume to maintain the battery below the operational temperature limit $T_{lim,op} = 45^{\circ}\mathrm{C}$, further supporting its compactness advantage.

Overall, this study demonstrates that integrating PCM within the cell mandrel is a promising approach for developing compact and efficient battery thermal management systems. The internal PCM configuration offers comparable thermal protection while improving spatial integration – an essential requirement for applications such as electric vehicles and portable electronics.

References

Afzal, A., *et al*. (2022), "Machine learning prediction and study of hotspots and hotspots location for sustainable battery energy system", *International Journal of Energy Research*, Vol. 46 No. 15, pp. 21045-21065, doi: 10.1002/er.8520.

Alkhedher, M., *et al*. (2024), "Electrochemical and thermal modeling of lithium-ion batteries: a review of coupled approaches for improved thermal performance and safety lithium-ion batteries", *Journal of Energy Storage*, Vol. 86, p. 111172, doi: 10.1016/J.EST.2024.111172.

Atalay, S., *et al*. (2020), "Theory of battery ageing in a lithium-ion battery: capacity fade, nonlinear ageing and lifetime prediction", *Journal of Power Sources*, Vol. 478, p. 229026, doi: 10.1016/J.JPOWSOUR.2020.229026.

Bernardi, D., Pawlikowski, E. and Newman, J. (1985), "A general energy balance for battery systems", *Journal of The Electrochemical Society*, Vol. 132 No. 1, pp. 5-12, doi: 10.1149/1.2113792.

Buonomo, B., *et al*. (2018), "Thermal cooling behaviors of lithium-ion batteries by metal foam with phase change materials", *Energy Procedia*, Vol. 148, pp. 1175-1182, doi: 10.1016/J.EGYPRO.2018.08.024.

Catalano, A.P., *et al*. (2023), "Thermo-Electrochemical FEM and circuit simulations of Li-Ion batteries", *IEEE Transactions on Components, Packaging and Manufacturing Technology*, Vol. 13 No. 8, pp. 1088-1095, doi: 10.1109/TCPMT.2023.3294702.

Chen, K., *et al*. (2024a), "An air-cooled system with a control strategy for efficient battery thermal management", *Applied Thermal Engineering*, Vol. 236, p. 121578, doi: 10.1016/J.APPLTHERMALENG.2023.121578.

Chen, Y., *et al*. (2024b), "Thermal management performance of lithium-ion batteries coupled with honeycomb array manifold and phase change materials under microgravity conditions", *Applied Thermal Engineering*, Vol. 251, p. 123586, doi: 10.1016/J.APPLTHERMALENG.2024.123586.

Cianciullo, M., *et al*. (2022), "Simulation of the thermal runaway onset in Li-Ion cells—influence of cathode materials and operating conditions", *Energies*, Vol. 15 No. 11, p. 4169, doi: 10.3390/en15114169.

Csemány, D. (2025), "Coupled thermal-electrical lumped parameter modeling of high-temperature sodium-sulfur battery", *Journal of Energy Storage*, Vol. 109, p. 115117, doi: 10.1016/J.EST.2024.115117.

Dileep, H., *et al*. (2024), "Thermal characterization of pouch cell using infrared thermography and electrochemical modelling for the design of effective battery thermal management system", *Applied Energy*, Vol. 376, p. 124301, doi: 10.1016/J.APENERGY.2024.124301.

Doyle, M., Fuller, T.F. and Newman, J. (1993), "Modeling of galvanostatic charge and discharge of the lithium/polymer/insertion cell", *Journal of The Electrochemical Society*, Vol. 140 No. 6, pp. 1526-1533, doi: 10.1149/1.2221597.

Feng, X., *et al*. (2019), "Investigating the thermal runaway mechanisms of lithium-ion batteries based on thermal analysis database", *Applied Energy*, Vol. 246, pp. 53-64, doi: 10.1016/J.APENERGY.2019.04.009.

Fragnito, A., *et al*. (2022), "Experimental and numerical analysis of a phase change material-based shell-and-tube heat exchanger for cold thermal energy storage", *Journal of Energy Storage*, Vol. 56, p. 105975, doi: 10.1016/J.EST.2022.105975.

Fuller, T.F., Doyle, M. and Newman, J. (1994), "Simulation and optimization of the dual lithium ion insertion cell", *Journal of The Electrochemical Society*, Vol. 141 No. 1, pp. 1-10, doi: 10.1149/1.2054684.

Goutam, S., *et al*. (2017), "Three-dimensional electro-thermal model of li-ion pouch cell: analysis and comparison of cell design factors and model assumptions", *Applied Thermal Engineering*, Vol. 126, pp. 796-808, doi: 10.1016/J.APPLTHERMALENG.2017.07.206.

Grandjean, T., *et al*. (2017), "Large format lithium ion pouch cell full thermal characterisation for improved electric vehicle thermal management", *Journal of Power Sources*, Vol. 359, pp. 215-225, doi: 10.1016/J.JPOWSOUR.2017.05.016.

Gu, W.B. and Wang, C.Y. (2000), "Thermal-electrochemical modeling of battery systems", *Journal of The Electrochemical Society*, Vol. 147 No. 8, pp. 2910, doi: 10.1149/1.1393625.

Hadjieva, M., Stoykov, R. and Filipova, T. (2000), "Composite salt-hydrate concrete system for building energy storage", *Renewable Energy*, Vol. 19 Nos 1-2, pp. 111-115, doi: 10.1016/S0960-1481(99)00024-5.

Huang, J., Xu, P. and Wang, P. (2020), "Experimental measurement of anisotropic thermal conductivity of 18650 lithium battery", *Journal of Physics: Conference Series*, Vol. 1509 No. 1, p. 12013, doi: 10.1088/1742-6596/1509/1/012013.

Jiang, K., *et al*. (2020), "Thermal management technology of power lithium-ion batteries based on the phase transition of materials: a review", *Journal of Energy Storage*, Vol. 32, p. 101816, doi: 10.1016/J.EST.2020.101816.

Jokar, A., *et al*. (2016), "Review of simplified pseudo-two-dimensional models of lithium-ion batteries", *Journal of Power Sources*, Vol. 327, pp. 44-55, doi: 10.1016/J.JPOWSOUR.2016.07.036.

Jordan, S.M., *et al*. (2024), "A new multiphysics modeling framework to simulate coupled electrochemical-thermal-electrical phenomena in Li-ion battery packs", *Applied Energy*, Vol. 360, p. 122746, doi: 10.1016/J.APENERGY.2024.122746.

Khan, M.M., *et al*. (2023), "Hybrid PCM-based thermal management for lithium-ion batteries: trends and challenges", *Journal of Energy Storage*, Vol. 73, p. 108775, doi: 10.1016/J.EST.2023.108775.

Landini, S., Leworthy, J. and O'Donovan, T.S. (2019), "A review of phase change materials for the thermal management and isothermalisation of lithium-ion cells", *Journal of Energy Storage*, Vol. 25, p. 100887, doi: 10.1016/J.EST.2019.100887.

Lee, N., *et al*. (2023), "Prognostic analysis of thermal interface material effects on anisotropic heat transfer characteristics and state of health of a 21700 cylindrical lithium-ion battery module", *Journal of Energy Storage*, Vol. 72, p. 108594, doi: 10.1016/J.EST.2023.108594.

Li, A., *et al*. (2020), "Reduced-order electro-thermal battery model ready for software-in-the-loop and hardware-in-the-loop BMS evaluation for an electric vehicle", *World Electric Vehicle Journal*, Vol. 11 No. 4, p. 75, doi: 10.3390/wevj11040075.

Lin, J., *et al*. (2021), "A review on recent progress, challenges and perspective of battery thermal management system", *International Journal of Heat and Mass Transfer*, Vol. 167, p. 120834, doi: 10.1016/J.IJHEATMASSTRANSFER.2020.120834.

Mallick, S. and Gayen, D. (2023), "Thermal behaviour and thermal runaway propagation in lithium-ion battery systems – a critical review", *Journal of Energy Storage*, Vol. 62, p. 106894, doi: 10.1016/J.EST.2023.106894.

Melcher, A., *et al*. (2016), "Modeling and simulation of the thermal runaway behavior of cylindrical Li-Ion cells—computing of critical parameters", *Energies*, Vol. 9 No. 4, p. 292, doi: 10.3390/en9040292.

Menale, C., *et al*. (2019), "Thermal management of lithium-ion batteries: an experimental investigation", *Energy*, Vol. 182, pp. 57-71, doi: 10.1016/J.ENERGY.2019.06.017.

Moynihan, C.T. (1966), "The temperature dependence of transport properties of ionic liquids. The conductance and viscosity of calcium nitrate tetrahydrate and sodium thiosulfate pentahydrate", *The Journal of Physical Chemistry*, Vol. 70 No. 11, pp. 3399-3403.

Nikolian, A., *et al*. (2016), "Lithium ion batteries-development of advanced electrical equivalent circuit models for nickel manganese cobalt lithium-ion", *Energies*, Vol. 9 No. 5, p. 360, doi: 10.3390/en9050360.

O'Regan, K., *et al*. (2022), "Thermal-electrochemical parameters of a high energy lithium-ion cylindrical battery", *Electrochimica Acta*, Vol. 425, p. 140700, doi: 10.1016/J.ELECTACTA.2022.140700.

Pilali, E., *et al*. (2025), "Passive thermal management systems with phase change material-based methods for lithium-ion batteries: a state-of-the-art review", *Journal of Power Sources*, Vol. 632, p. 236345, doi: 10.1016/J.JPOWSOUR.2025.236345.

Rao, L. and Newman, J. (1997), "Heat-generation rate and general energy balance for insertion battery systems", *Journal of The Electrochemical Society*, Vol. 144 No. 8, pp. 2697-2704, doi: 10.1149/1.1837884.

Rodrigues, M.-T.F., *et al*. (2017), "A materials perspective on Li-ion batteries at extreme temperatures", *Nature Energy*, Vol. 2 No. 8, p. 17108, doi: 10.1038/nenergy.2017.108.

Saw, L.H., Ye, Y. and Tay, A.A.O. (2013), "Electrochemical–thermal analysis of 18650 lithium iron phosphate cell", *Energy Conversion and Management*, Vol. 75, pp. 162-174, doi: 10.1016/J.ENCONMAN.2013.05.040.

Su, Q., *et al*. (2025), "Experimental investigation of a thermal management device based on a novel thin heat-pipe array for energy storage battery packs", *International Communications in Heat and Mass Transfer*, Vol. 161, p. 108486, doi: 10.1016/J.ICHEATMASSTRANSFER.2024.108486.

Sutheesh, P.M., *et al*. (2024), "Numerical investigations on thermal performance of PCM-based lithium-ion battery thermal management system equipped with advanced honeycomb structures", *International Communications in Heat and Mass Transfer*, Vol. 158, p. 107937, doi: 10.1016/J.ICHEATMASSTRANSFER.2024.107937.

Taheri, P., Yazdanpour, M. and Bahrami, M. (2013), "Transient three-dimensional thermal model for batteries with thin electrodes", *Journal of Power Sources*, Vol. 243, pp. 280-289, doi: 10.1016/J.JPOWSOUR.2013.05.175.

Veza, I., *et al*. (2024), "Electric vehicle (EV) review: Bibliometric analysis of electric vehicle trend, policy, Lithium-Ion battery, battery management, charging infrastructure, smart charging, and electric vehicle-to-everything (V2X)", *Energies*, Vol. 17 No. 15, p. 3786, doi: 10.3390/en17153786.

Vyas, D., *et al*. (2024), "Investigation on thermal management of 18650 Lithium-Ion batteries using nano-enhanced paraffin wax: a combined numerical and experimental study", *Arabian Journal for Science and Engineering*, Vol. 49 No. 11, pp. 15565-15582, doi: 10.1007/s13369-024-09122-2.

Williams, N.P., Trimble, D. and O'Shaughnessy, S.M. (2024), "An experimental investigation of liquid immersion cooling of a four cell lithium-ion battery module", *Journal of Energy Storage*, Vol. 86, p. 111289, doi: 10.1016/J.EST.2024.111289.

Wu, C., *et al*. (2024), "A review on the liquid cooling thermal management system of lithium-ion batteries", *Applied Energy*, Vol. 375, p. 124173, doi: 10.1016/J.APENERGY.2024.124173.

Yang, Y., *et al*. (2018), "Battery energy storage system size determination in renewable energy systems: a review", *Renewable and Sustainable Energy Reviews*, Vol. 91, pp. 109-125, doi: 10.1016/J.RSER.2018.03.047.

Zhang, D., Popov, B.N. and White, R.E. (2000), "Modeling lithium intercalation of a single spinel particle under potentiodynamic control", *Journal of The Electrochemical Society*, Vol. 147 No. 3, p. 831, doi: 10.1149/1.1393279.

Zhang, F., *et al*. (2023), "Thermal performance analysis of a new type of branch-fin enhanced battery thermal management PCM module", *Renewable Energy*, Vol. 206, pp. 1049-1063, doi: 10.1016/J.RENENE.2023.02.083.

Zhao, C., *et al*. (2020), "Hybrid battery thermal management system in electrical vehicles: a review", *Energies*, Vol. 13 No. 23, p. 6257, doi: 10.3390/en13236257.

Zhuang, Y., *et al*. (2021), "Thermal uniformity performance of a hybrid battery thermal management system using phase change material and cooling plates arrayed in the manner of honeycomb", *Thermal Science and Engineering Progress*, Vol. 26, p. 101094, doi: 10.1016/J.TSEP.2021.101094.

Corresponding author
Francesco Piccirillo can be contacted at: francesco.piccirillo@unina.it